Chemical Papers (2021) 75:6575–6589
https://doi.org/10.1007/s11696-021-01830-5

ORIGINAL PAPER

Polypyrrole/functionalized multi-walled carbon nanotube composite for optoelectronic device application

M. Zwawi[1] · A. Attar[1] · A. F. Al-Hossainy[2] · M. H. Abdel-Aziz[3,4] · M. Sh. Zoromba[3,5]

Received: 4 June 2021 / Accepted: 18 August 2021 / Published online: 22 August 2021

Abstract
Doped polypyrrole/functionalized multi-walled carbon nanotubes composites were synthesized in an acidic medium using an in situ oxidative polymerization route. $FeCl_3$ was utilized as an oxidizing agent and sodium dodecyl sulfate as a surfactant to produce 2-dimensional films. Thin films were fabricated from polypyrrole/functionalized multi-walled carbon nanotubes composites using the thermal evaporation technique and are inspected by various methods. The surface morphology of the thin film is characterized by computing the crystalline size and shape. The XRD study of [PPy] and $[PPyCNs]^{NC}$ as-deposited thin films showed that these polymers are merely a triclinic crystal structure with a space group $P\bar{1}$. The crystallite size (D) value average is 74.24 nm for $[PPyCNsF]^{NC}$. The direct energy gap values are decreased from 2.68 to 1.93 eV for [PPy] and $[PPyCNs]^{NC}$ as-deposited thin film, respectively. The optical features of the thin film were investigated. The optical constants and optical conductivity for the nanotubes composites were figured and interrelated by using experiment and TDDFT-DFT/$DMOl^3$ simulation methods. The structural and optical parameters of the simulated nanocomposites as single isolated molecules are in reasonable agreement with the investigational work. The nanotube composite thin films exhibited encouraging results to be a worthy applicant for polymer solar cell requests.

Keywords Polypyrrole nanotubes · Nanotube composites · Thin film · TDDFT-DFT · Optoelectrical device

Introduction

The conducting polymers (CPs) have recently demonstrated massive curiosity because of their exciting optoelectronic properties. CPs are conjugated polymers that are highly absorbable, electrochemically active, conductive, and chemically stable (Krishnaswamy et al. 2019). Because of their distinct physical and chemical structures, they exhibit significant optical and electrical capabilities in a variety of applications, including electrochromic systems, emitting diodes, light photovoltaics, microwave shielding, electrodes for batteries, and sensors (Yadav et al. 2018; Cho et al. 2005; Jiang et al. 2005). Polypyrrole (PPy) is one of the conducting polymers with greater environmental stability and conductivity than many other conducting polymers. Commercial applications of PPy include biosensors (Vidal et al. 1999; Campbell et al. 1999; Sedahmed et al. 2011; Abdel-Aziz et al. 2013), gas sensors (Kincal et al. 1998; Kemp et al. 1999), microactuators (Smela 1999), anti-electrostatic coatings (Liang et al. 2017), polymeric batteries, electronic equipment, and functional films (Munish and Badlani 2019). PPy coatings offer high thermal stability and can be used in carbon composites (Iroh and Williams 1999; El-Ashtoukhy and Abdel-Aziz 2013). There are two methods for converting PPy from an insulator to a polymer conductor. The first approach involves doping PPy with reducing chemicals, which supply electrons to the empty bands of the polymer chains. It results in the formation of negatively charged carriers. The second doping approach involves utilizing

✉ M. H. Abdel-Aziz
helmy2002@gmail.com

1 Mechanical Engineering Department, King Abdulaziz University, Rabigh 21911, Saudi Arabia

2 Chemistry Department, Faculty of Science, New Valley University, Al-Kharga, Al-Wadi Al-Gadid, Kharga 72511, Egypt

3 Chemical and Materials Engineering Department, King Abdulaziz University, Rabigh 21911, Saudi Arabia

4 Chemical Engineering Department, Faculty of Engineering, Alexandria University, Alexandria, Egypt

5 Chemistry Department, Faculty of Science, Port-Said University, 23 December Street, Port-Said 42521, Egypt

oxidizing chemicals as dopants, which withdraw electrons from polymer chains to produce positive charges. These positive charges act as P-type material. Therefore, P-type doping is favored and displayed more importance in both fundamental research and its potential applications (Alcacer 1987). Carbon nanotubes (CNTs), on the other hand, have been widely employed as fillers, particularly in desirable combinations with conducting polymers. This is due to their great chemical stability, electrical conductivity, and surface area (Siwal et al. 2020; Endo et al. 2003; Heer et al. 2005). Polymer/CNTs composites have grabbed the interest of many researchers, because they may include unique combinations with better capabilities than the separate components (Liu et al. 2005; Wang et al. 2005; Sanghvi et al. 2005; Zhang et al. 2011; Ma et al. 2008; De et al. 2009). Herein, doped polypyrrole/functional multi-walled carbon nanotubes composites were produced using in situ oxidative polymerization means by anhydrous ferric chloride initiator in the presence of SDS surfactant to control the morphology of the resulting polypyrrole (2-dimensions). Thin films were fabricated from polypyrrole/functionalized multi-walled carbon nanotubes composites using the thermal evaporation technique.

Table 1 Specifications of MWCNTs

Specifications	–COOH MWCNTS
Supplier	Grafen Turkey
Color	Gray
C-Purity	93.83%
Density	215 kg/m^3
Specific surface area	25 m^2/g
Zeta potential	− 20 to 39.7 mV

Experimental section

Raw materials

Except for pyrrole distillation, all products have been utilized without further purification. Acros Organics supplied sodium dodecyl sulfate (SDS), ethanol (Aldrich), anhydrous dimethyl formaldehyde (DMF), dimethyl sulfoxide (DMSO), isopropyl alcohol (Aldrich), and anhydrous ferric chloride (Aldrich). Hydrochloric acid, hydrofluoric acid, nitric acid, a single crystalline (p-Si) were bought from Sigma-Aldrich, chromic acid (sulfuric acid combined with 25 ml of a saturated aqueous solution of chromium trioxide) (Sigma-Aldrich). Grafen Co., Turkey, provided the carboxylic functionalized multi-walled carbon nanotubes (MWCNTs). Table 1 lists the specifications of FMWCNTs (-COOH MWCNTs). Table 2 shows the description of the equipment used in the fabrication and analysis of the composites.

Synthesis of polypyrrole/FMWCNTs composites

3.5 g sodium dodecyl sulfate (SDS) was dissolved in 100 mL absolute ethanol. This solution was diluted by distilled water up to 400 mL using a magnetic stirrer (850 rpm) at room temperature; 0.8 g of carboxylic functionalized multi-walled carbon nanotubes was added to the previous solution; 4 mL pyrrole monomer was added to the above dispersion followed by an ultrasonic homogenizer for 20 min; 160 mL (0.5 M $FeCl_3$) was added drop by drop to the dispersion for 45 min. Polypyrrole progressively developed during the addition step, which occurs in the presence of FMWCNTs during the polymerization process. Following the completion of the initiator addition, the resultant dispersion was placed under a magnetic stirrer for an additional 1 h. The resultant dispersion was allowed to settle overnight. The mixture was then filtered and rinsed with distilled water

Table 2 Equipment and methods used in fabrication and analysis of the composites

Methods/Analysis	Equipment model
Thermal evaporation	The UNIVEX 250 Leybold (Germany), two tantalum boats with no vacuum rupture, and a deposition average of 3 Å/s were used
FT-IR	Perkin – Elmer FT-IR type 1650 spectrophotometers reported infrared spectra
SEM	Scanning electron microscope (SEM; Inspection S, FEI, Holland) at 3 kV determined the morphology of the copolymer surfaces
Film thickness	Film thickness is determined by using a Digital micrometer with accuracy $\pm 10^{-3}$ nm
XRD	An X-ray diffractometer (model X'pert) of Philips with monochromatic Cu Kα radiation studied the average crystallites size in the copolymer matrix
UV	The spectra determinations of the fabricated thin films were determined by utilizing SHIMADZU UV-3101 UV–Vis–NIR

before being treated with ethanol. The final composite was cured for two days at 60 ˚C.

Fabrication thin film

The thin film polypyrrole [PPy]^{TF} and nanocomposite thin film [PPyCNsF]^{NC} were made up to examine the greatest conductivity. Thin films on washed quartz substrates by chromic acid/deionized water are produced with a high vacuum coating system by standard thermal evaporation at a vapor pressure of about 5×10^{-5} mbar. The UNIVEX 250 Leybold (Germany), two tantalum boats with no vacuum rupture, and a deposition average of 3 Å/s were used (Al-Hossainy et al. 2019; Torraca et al. 2018). The UNIVEX 250 Leybold crystalline quartz micro-balance for film thickness is illustrated in Fig. 1a, with a length of approximately 200 nm. Figure 1b depicts the various steps involved in the preparation of [PPy/FMWCNTs] nanocomposites utilizing ferric chloride and the in situ polymerization process.

Computational study

According to DFT analysis, the product of CATSTEP and DMol^3 scheming was used to evaluate the utility of [PPyCNsF]^{NC} molecular structures and frequency measurements in the gas stage. The proof estimated by functional PBE and GGA exchanges, natural pseudo-conservative potential, and base range of DNPs, programmed for tolerable molecules, was calculated by DMol^3 and CATSTEP accordingly (Lin et al. 2010). The degree of the plane-wave amputates capacity used in computer simulations was 830 eV. XRD and optical functions were constructed using the DMol^3, physical and spectroscopic [PPyCNsF]^{NC}, and the CATSTEP frequency was approximated. In combination with non-local needs, a practical interaction between Becker and Lee-Yang Parr (B3LYP/WBX97XD/6-311G) has been formed in terms of enhanced shapes and vibration (IR) levels of doped [PPyCNsF]^{NC} in the gas state (Shuller-Nickles et al. 2014; Gill et al. 1992). The programmed GAUSSIAN 09 W Structure explores symmetry variables, enhanced layouts, vibration, and vitality of nanocomposite combinations. The DFT scheme based on the WBX97xd/6–311 G B3LYP technology has created several earnest consequences in studies published by our community for the configuration-spectrum relationship (Ibrahim and Al-Hossainy 2021) which contains a range of important experimental results. The Distance approach is used to approximate the doped representations of Gaussian and Castep [PPyCNsF]^{NC} in the gas process, an intentional plurality of descriptors,

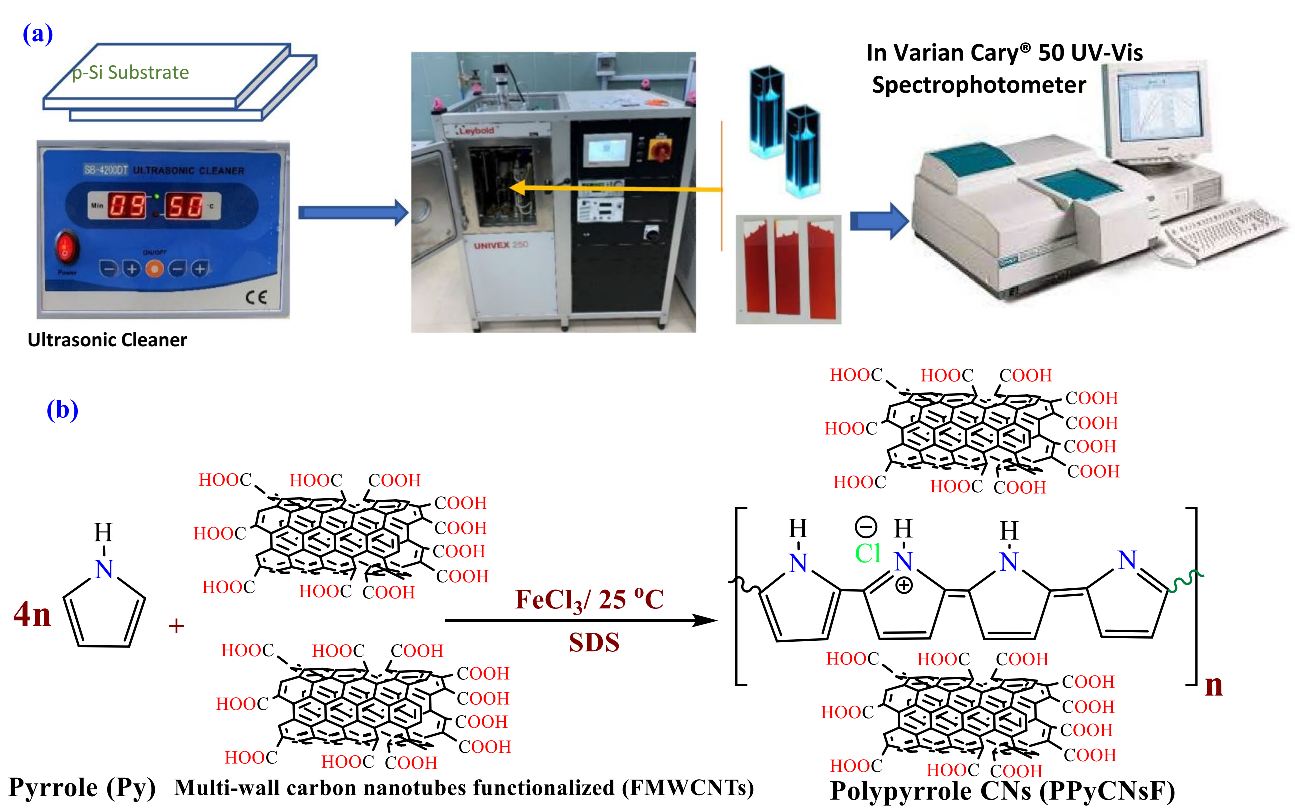

Fig. 1 Fabrication of [PPyCNsF]^{NC} by using physical vapor deposition (PVD) and chemical structure of [PPyCNsF]^{NC} thin films

prototypical knowledge on total energy, and the cumulative use of several versions of different complexity (Abd-Elmageed et al. 2020).

Results and discussion

FT-IR spectroscopy

The FT-IR spectroscopy was performed to define the functional groups in the structural backbone for [CNsF]^{NPs}, [PPy], and [PPyCNsF]^{NC} thin film which is shown in Fig. 2a–c. From Fig. 2c, the [PPyCNsF]^{NC} thin-film performed the broadening vibration of absorption bands at 1109 cm^{-1}, which is recognized to ν(C–O). In the range 3200–3600 cm^{-1}, the absorption band was identified, and this is owed to O–H trembling (Abdel-Aziz et al. 2020a). Additionally, the distinctive bands of the resultant nanocomposite [PPyCNsF]^{NC} thin film are represented in FT-IR spectroscopy. The spectrum of the thin films [PPyCNsF]^{NC} revealed this hydrogen bonding among (–NH) groups of polymers produced and [PPyCNsF]^{NC} groups of thin films [PPyCNSF]NC groups. Conversely, the Gaussian 09 W program framework on the WBX97XD for the [PPyCNsF]^{NC} gassy process in the isolated molecule matrix is shown in Fig. 2 for the measured IR range at 6-311G/DFT. The resulting DFT-Gaussian 09 W vibration figures are very analogous to experimental findings. The corresponding vibration bands are very analogous to the investigational outcomes (Badr et al. 2006; Reddy et al. 2019). The [PyCNsF]NC gaseous step of the isolating molecule backbone as seen in Fig. 2d can be established on the measured data from the experiments and the 09 W/DFT program package.

The theoretical IR spectrum of [PPyCNsF]^{NC} gasses in the isolated molecule was predicted to have spectroscopic

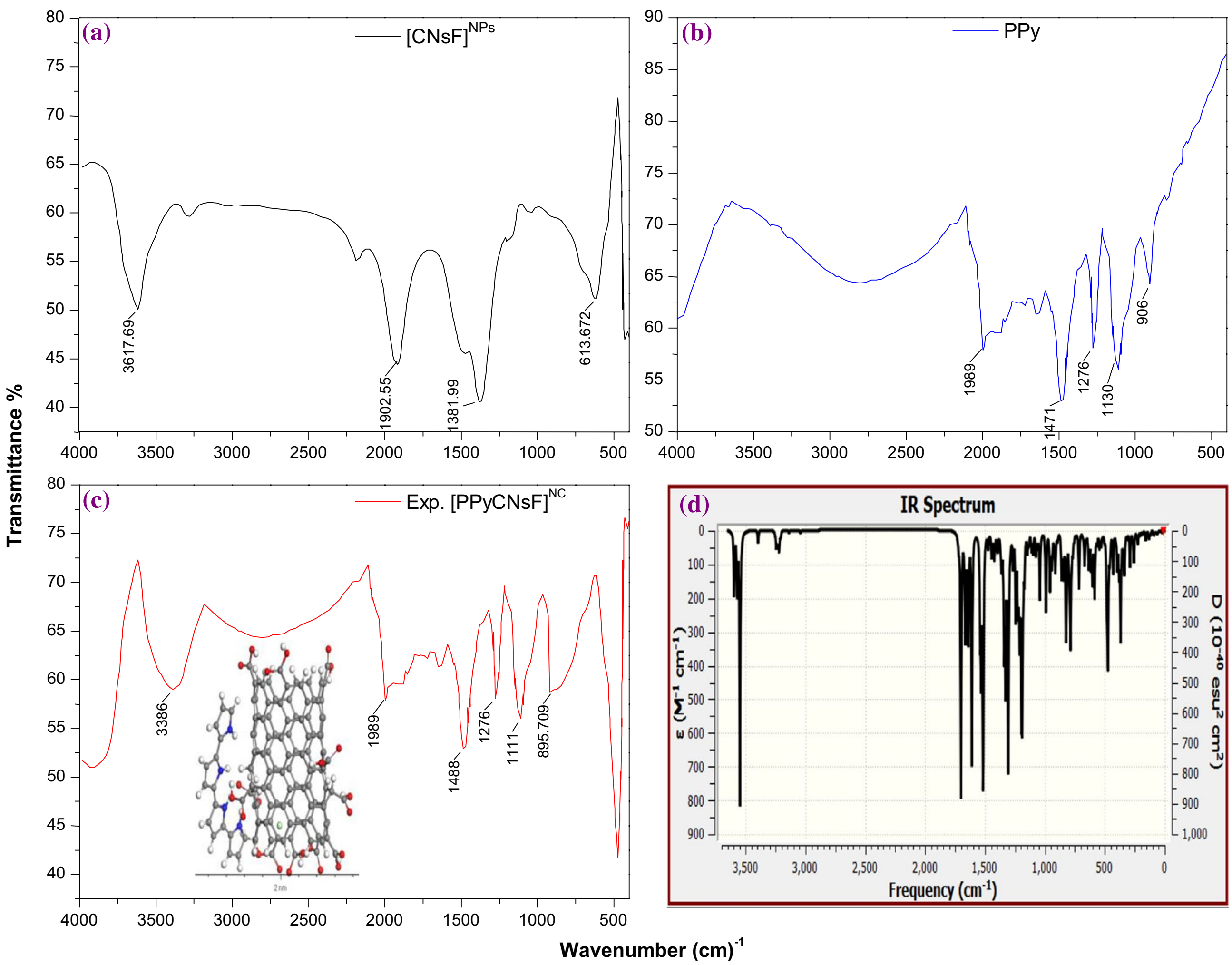

Fig. 2 **a** Experimental IR spectrum for [CNsF]^{NPs}; **b** Experimental IR spectrum for [PPy]; **c** Experimental IR spectrum for [PPyCNsF]^{NC} and **d** Simulated IR spectrum for [PPyCNsF]^{NC} by using *Gaussian/ DFT* method

signs. Figure 2 shows the minor variations between the expected and observed frequencies. The key intention behind the differentiation was to conduct the count in a vacuum while the calculations for the solid-state were done. The dynamic nature of the vibratory modes of the ligands investigated indicates that the torsion is weak and because the decryption of the ring modes besides the imitative is difficult to allocate to all plane modes. However, the existence of such apparent vibrations is to be seen in the graph obtained (Al-Hossainy and Ibrahim 2015a; Awad et al. 2004). The direct correlation between the calculated $\left(\lambda_{\text{Cal.}}\right)$ and experimental wavenumbers $\left(\lambda_{\text{Exp.}}\right)$ is described by the following equation for $[\text{PPyCNsF}]^{\text{NC}}$ gaseous phase of an isolated molecule

$$\lambda_{\text{Cal.}} = 0.971\lambda_{\text{Exp.}} + 20.75 \tag{1}$$

with correlation coefficients ($R^2 = 0.988$).

Surface morphology study of the thin film

The surface morphology and nanostructure form of the synthesized neat PPy was investigated by the SEM technique. The obtained SEM images are represented in Fig. 3a and b. These SEM images show that the PPy structures are produced in a 2-dimensional film. These films are composing fine nanoparticles impeded in the film. The shape and size of the resulting polymer depend on the type of used surfactant during the polymerization process. The formation of PPy sheet/films in the presence of SDS using $FeCl_3$ as an oxidizing agent was reported by Gangopadhyay (2013) (dissolved in a water medium), but it is stated that the films are too brittle to handle freely. This perhaps might be due to the absence of ethanol as a cosolvent or might be due to the variations in the molar ratios of the pyrrole and surfactants/oxidants, which might affect the bonding between the formed PPy chains. Figure 3c and d show SEM of the

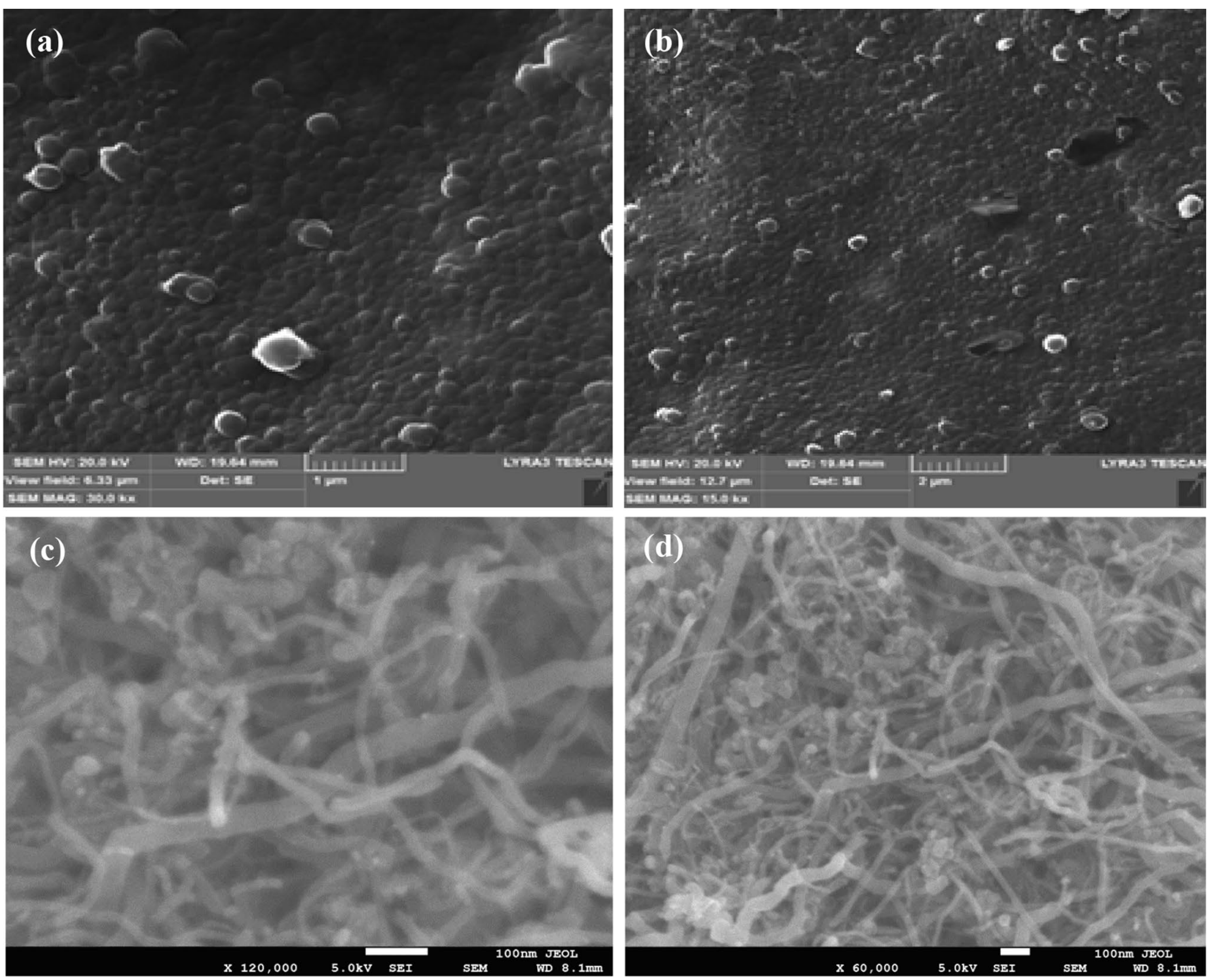

Fig. 3 **a**-**b** SEM image of the as-synthesized [PPy] thin film at 1 µm and 2 µm magnifications. **c**-**d** $[\text{PPyCNsF}]^{\text{NC}}$ thin film at 100 nm

resulting FMWCNTs coated with PPy at two different magnifications. It can be observed the nanotubes of carbon through the resulting composite after being coated by polypyrrole polymer.

XRD of $[PPyCNsF]^{NC}$ thin film

The XRD pattern reveals the long-range order and the crystallinity of the doped $[PPyCNsF]^{NC}$ thin film with a sharp peak series of $5^{\circ} < 2\theta < 45^{\circ}$ ranges as displayed in Fig. 4a–b. Moreover, x-ray diffraction appears to suggest that the thin film matrix is distributed to the consistent one. The polyclinic structure with Triclinic symmetry/$P\overline{1}$ based on database_code_amcsd 0,020,331 is seen in both thin-film and gas phases (Kampf et al. 2014). $[PPyCNsF]^{NC}$ thin film, XRD configuration includes a sharp top in the region $5^{\circ} < 2\theta < 45^{\circ}$ showing a long-range setting and crystallinity. In addition, $[PPyCNsF]^{NC}$ thin-film matrix displays the XRD patterns as evidence of homogeneous distribution. The XRD configuration exhibited the identical diffraction peaks with variable intensity Sect. $5° \geq 2\theta \geq 28°$ located at 6.95°, 11.65°, 16.24°, 17.71°, 19.30°, 22.21°, 25.24°, 26.86°, 28.23° and 31.35° for $[PPyCNsF]^{NC}$ thin-film matrix. The measurement method Crystal Sleuth Microsoft and Polymorph calculate the maximum online diffraction values in relation to the expected information. The calculated crystallinity parameters for the application refinement type 3.0, the mean crystallite scale (D), the Miller index (Hkl), and full width at half-maximum (FWHM) are given in Table 3 by applying Kurt Barthelme's & Bob Downs program application. Application *Scherrer* equation, the range of Bragg angle $5 \leq 2\theta \leq 45$, the range 1/$d_{hkl} = 0.0566$ Å^{-1}–0.7446 Å^{-1}, $\lambda = 1.540562$ Å, source copper, $I_2/I_1 = 0.5$, *Pseudo-Voigt function* to figured XRD for doped $[PPyCNsF]^{NC}$ using polarization = 0.5. The D_{avarge} of doped $[PPyCNsF]^{NC}$ thin film has been dogged employing Debye -Scherer's equation.

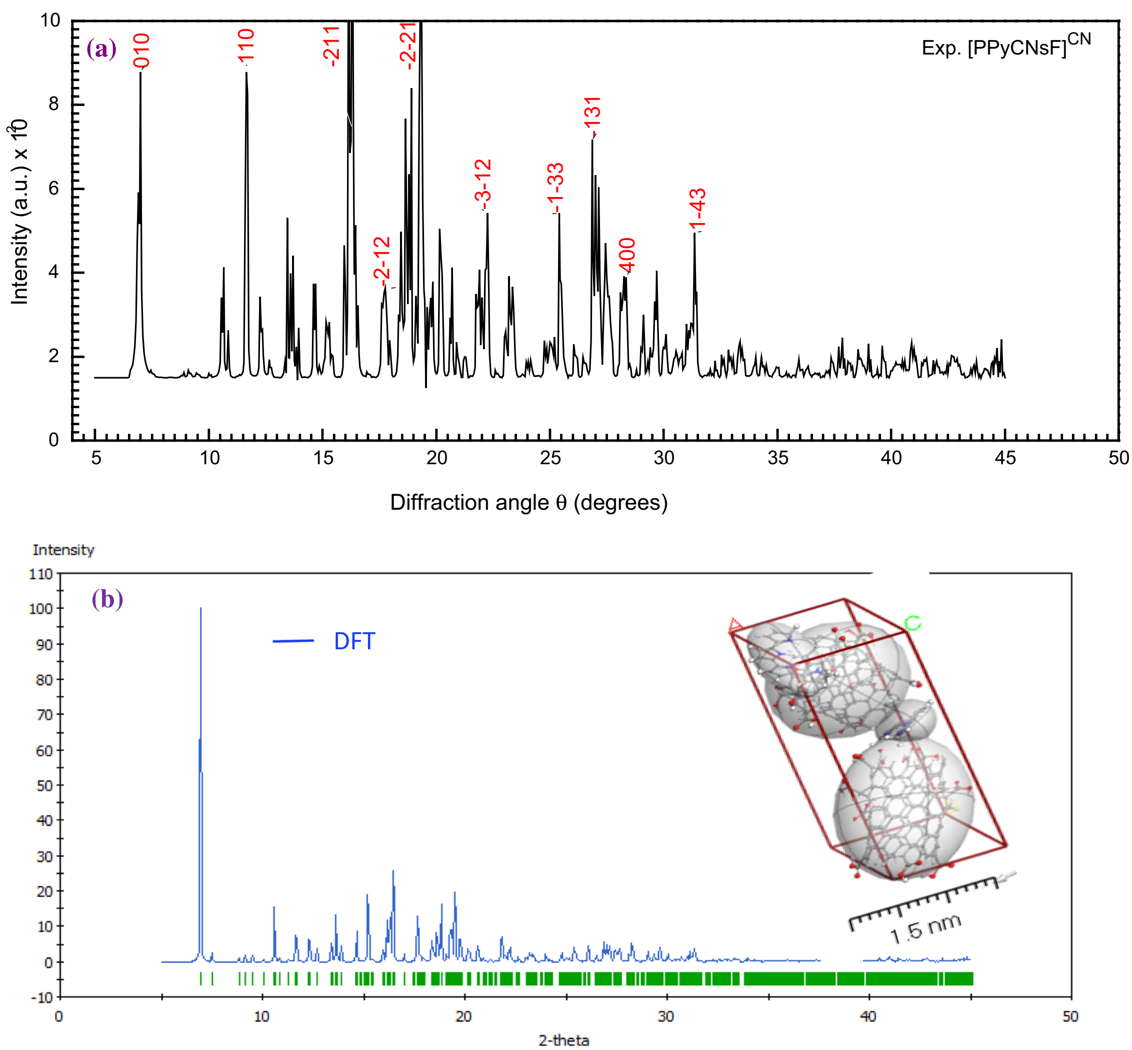

Fig. 4 **a-b** Combined experimental of $[PPyCNsF]^{NC}$ thin film and simulated XRD patterns of $[PPyCNsF]^{NC}$ as isolated molecule in gaseous state

Table 3 The computed crystallinity parameters for $[PPyCNsF]^{NC}$ thin film at λ = 1.54 Å, machine error = -0.162

Symmetry	Observed				Computed				
	2θ (°)	d (Å)	hkl	FWHM	2θ (°)	d (Å)	Δ(θ)	Δd	D_{Av} [b]
[PPyCNsF]NC thin film	6.950	13.0	010	0.2410	7.58	11.91	0.624	1.0937	34.52
TRICLINC	11.65	7.69	110	0.1286	11.35	7.903	−0.306	−0.209	64.91
a = c = 13.64 (9); b = 13.50 (2)	16.24	5.51	−211	0.3181	16.25	5.504	0.010	0.0035	26.37
α = 115.7 (5); β = 107.9 (6),	17.71	5.05	−2–12	0.2291	17.71	5.049	0.003	0.0009	36.68
γ = 92.6(7)°	19.30	4.63	−2–21	0.1485	19.32	4.629	0.014	0.0033	56.72
V = 1800 (22);	22.21	4.03	−3–12	0.1591	22.16	4.036	−0.056	−0.008	53.19
Rmse [a] = 0.00075152998	25.42	3.52	−1–33	0.0532	25.46	3.518	0.041	0.0056	160.01
	26.86	3.34	−131	0.0527	26.86	3.337	−0.008	−0.001	162.00
	28.23	3.18	400	0.2617	28.25	3.174	0.023	0.0026	32.72
	31.35	2.87	1–43	0.0748	31.33	2.867	−0.021	−0.0019	115.30
Average				0.16668					74.24

[a] Root-mean-square error and [b] nm

$$D_{average} = \frac{0.9\lambda}{\text{FWHM}\ \cos\theta} \tag{2}$$

where (λ = 0.154 nm), θ the matching 2θ and the FWHM (in radians) (Almutlaq et al. 2021; Rajeh et al. 2019; Mahmoud et al. 2020). The crystallite size (D) value average is 74.24 nm for $[PPyCNsF]^{NC}$. The polymorphic PXRD studies are compared with the PXRD equations of the associated practical X-ray configuration. In the PXRD measured and/or experimentally finished film portion, there are small variations in the strength and position values of specific peaks. Besides the data processing and instrumentation features, several parameters for defining microstructural samples such as their size, form, and path of distribution of the crystallites in the powder may affect the PXRD testing pattern.

$[PPyCNsF]^{NC}$ simulated a polycrystalline nature place and created a triclinic alignment with the $P\overline{1}$ space group. $[PPyCNsF]^{NC}$ chief peak/2θ = 16.24°, the qualitative distinction relies on visual assessment and the accuracy of computations PXRD for polymorphs and experimental trends. [PPyCNSF]NC key peak/2θ = 16,24°, a consistency comparison relies on a visual assessment to detect a strong agreement on both polymorphs and experimental patterns between computed PXRD (Grzelak et al. 2017; Almutlaq and Al-Hossainy 2020; Bersani et al. 2016).

XPS measurements

XPS measurements should be performed to obtain information about the type of functional groups and their quantitative share. The results of these works should be included in the theoretical model. The XPS elemental analysis and their atomic percentage are also shown in Fig. 5a–b.

The XPS survey profiles of the FMWCNTs and PPy/FMWCNTs composite are shown in Fig. 6a–b. The C1s and O1s OKLL peaks could be observed in the spectra of the neat of both FMWCNTs and PPy/FMWCNTs composite. A weak Cl_2p and S_2P bands were observed at around 200 eV for

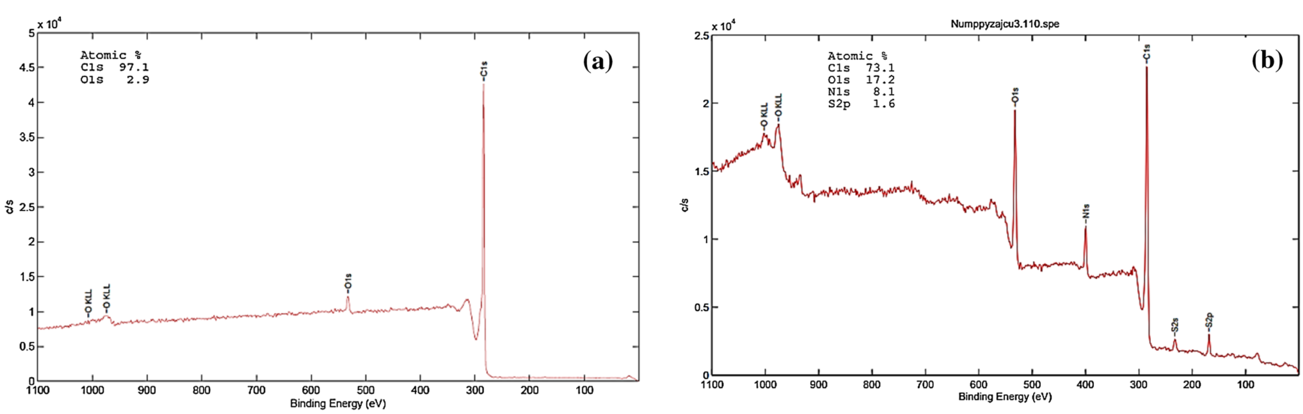

Fig. 5 Typical XPS survey profiles of **a** FMWCNTs and **b** PPy/ MWCNTs composite

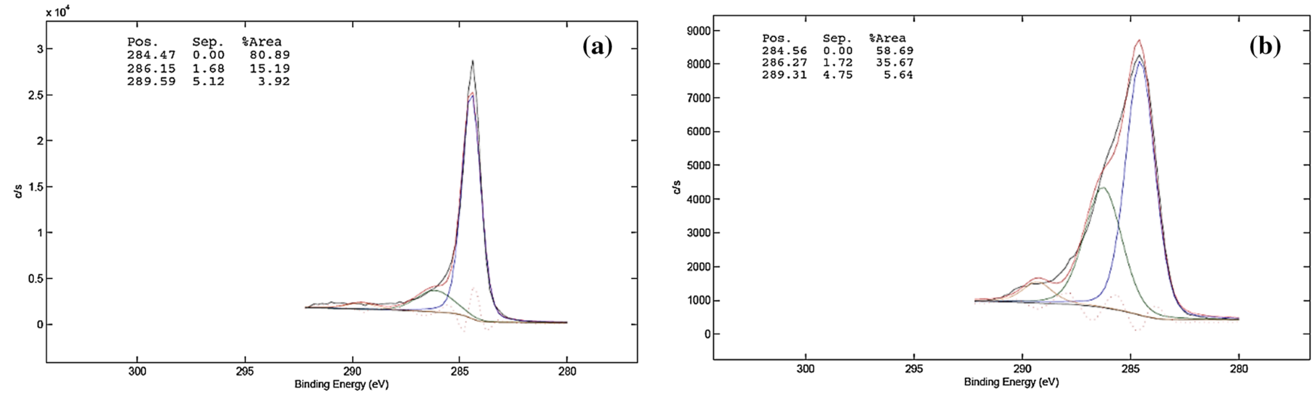

Fig. 6 XPS profiles of **a** FMWCNTs and **b** PPy/FMWCNTs composite

PPy/MWCNTs composite. These peaks are due to the chloride ion doped from $FeCl_3$ oxidizing agent and sulfur gained from SDS surfactant during the polymerization process. The C1s/O1s ratio of the neat FMWCNTs is higher than that of the PPy/FMWCNts composite. The intensity of the O1s band decreased slightly for the PPy/MWCNTs composites. This indicates the success of doping with chloride ions for the PPy chains during the polymerization process. The C1s XPS profiles of FMWCNTs and PPy/MWCNTs composites are represented in Fig. 6a and b. As shown in Fig. 6a, the observed three peaks at 284.47, 286.15 and 289.59 eV are occupied areas of 80.89%, 15.19%, and 3.92%, respectively, for neat FMWCNTs while the observed peaks (Fig. 6b) for the composite at 284.56, 286.27 and 289.31 eV are occupied areas of 58.69%, 35.67%, and 5.64%, respectively, for PPy/FMWCNTs composite. The spectra of the coated FMWCNTs by PPy in the current composite are nearly similar to the spectra of the uncoated FMWCNTs. There are no significant changes observed in the peak positions. This confirms that PPy has successfully coated MWCNTs with no extra bonds or crosslinking in the contact surfaces. The excellent π-π stacking between PPy backbones and FMWCNTs might also assist in stabilizing.

Geometry Study for [PPy] and $[PPyCNsF]^{NC}$ as an isolated molecule

The 3D plots of electron density and potential come to be realistic in most computations with the DNP basis sets for [PPy] and $[PPyCNsF]^{NC}$ as isolated molecules are shown in Fig. 7a–d, respectively. In all calculations, the negative electrostatic potential is visible and symmetrically distributed in respect to the macrocyclic plane, while both positive and negative lobe form varies according to the basis set. As was detected in our previous theoretical experiments of the interactions of the [PPy] open cyclic keto dyes with the $[CNs]^{NPs}$ nanoparticles moiety to form the closed cyclic, the negative lobe contacting carbon nanocluster contracts though the opposite one expands (Hashim et al. 2020; Abdel-Aziz et al. 2020b).

In addition, the electrostatic potential maps (MEP) are an electrostatic potentials trace mapped at a constant electron density surface with *DMOl*^{3}. Figure 7e–f are often too significant for research into the physicochemical relationship of molecular structure with a red color. The highest negative region for the electrophilic attack site and blue color express the maximum positive region that is the favored nucleophilic attack site. The potential is following red < green < blue, the most desirable being blue. The remarked 3D of MEP_{Vmin} minimum principles neighboring the lone pair area of [PPy] and $[PPyCNsF]^{NC}$ as isolated molecules are -1.046×10^{-1} and -1.476×10^{-1} kcal/mol done by MEP structure calculation, respectively (Veved et al. 2020; Ibrahim et al. 2020a). The calculated values of MEP_{Vmax} of the nanocomposite and hybrid nanocomposite derivatives as a gaseous phase molecule are $+2.436$ and $+5.465\times10^{-1}$ kcal/mol done by *DMOl*^{3}*/DFT computations,* respectively. As predicted, the $MEPV_{min}$ and $MEPV_{max}$ values should be calculated by electronically substituted magnitudes. The MEP_{Vmax} negative amount (-1.046×10^{-1} kcal/mol) is found for the [PPy] as an isolated molecule. The positive value of $MEPV_{max}$ (2.436 kcal/mol) functioned as an important quantitative predictor for the single couple (Mohlala et al. 2020; Al-Hossainy and Eid 2020). $MEPV_{min}$ may be more instrumental and straightforward than techniques based on $\nu(C=O)$ values relying on quantification of electronic results of dies. $MEPV_{max}$ can be used as σ-donor power to the [PPy] derivatives movement $[PPyCNsF]^{NC}$ as an isolated molecule matrix.

If no major π-back bonding of [PPy] as an isolated molecule is present, the energy interaction between nanoparticles [PPy] and $[CNs]^{NPs}$ is directly proportional to the value of $MEPV_{max}$ (Lim et al. 2020; Zoromba et al. 2019).

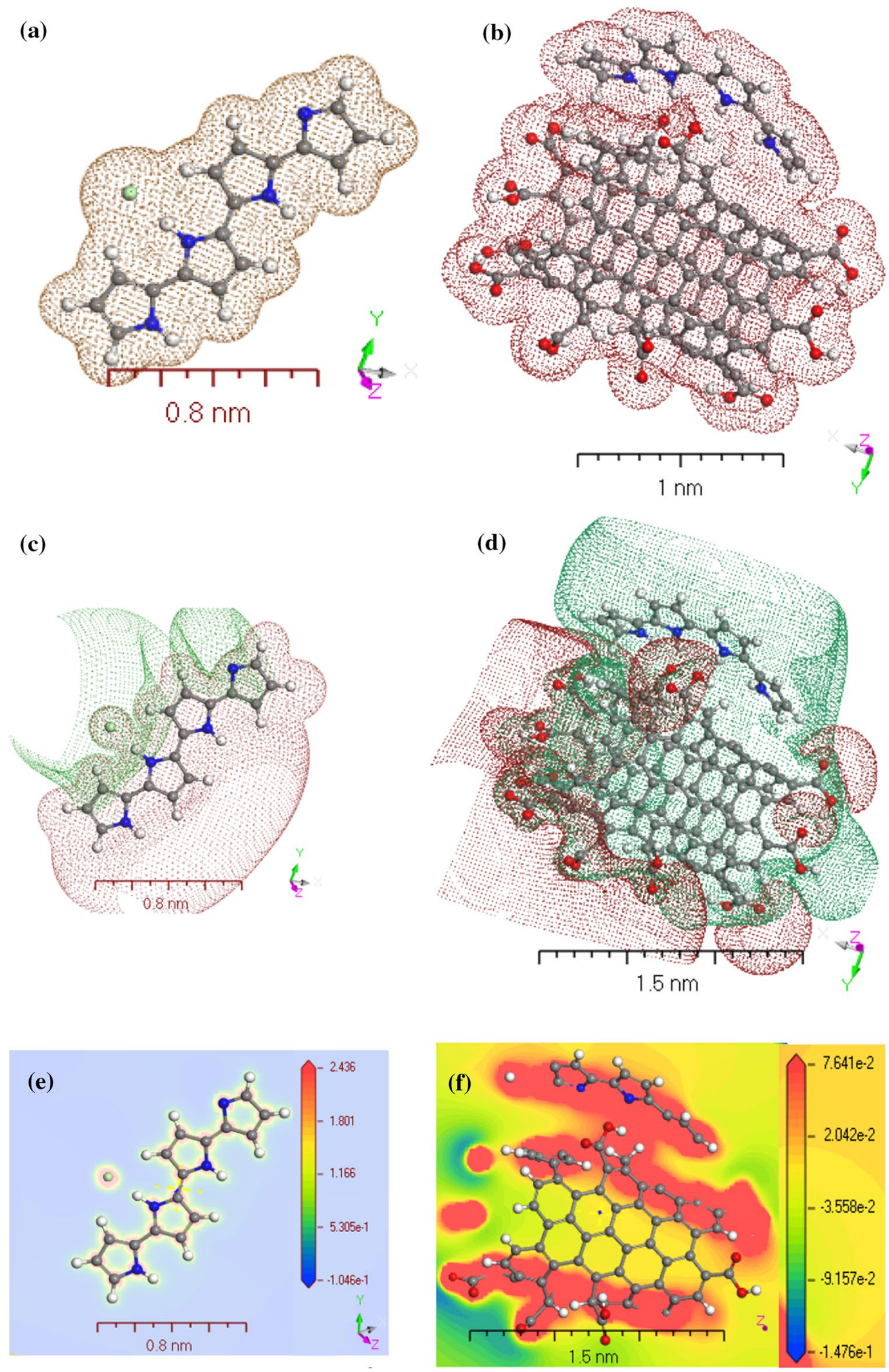

Fig. 7 The DFT computation used DMOl[3] Material studio software programs of **a** Electron density of the [PPy]; **b** Electron density of the [PPyCNsF]^{NC} **c** Potentials of the [PPy]; **d** Potentials of the [PPyCNs]^{NC}; **e** MEP of the [PPy] and **f** MEP of the [PPyCNs]^{NC} gaseous phase as isolated molecule

The computed HOMO and LUMO for [PPy] and [PPyCNs]^{NC}

The molecular structures along with atomic numbering of [PPy] and [PPyCNsF]^{NC} as well as their nanocomposites are shown in Fig. 6a–b. The bond length and angle of the [PPy] and [PPyCNsF]^{NC} as isolated molecules are supplied in Table 4. The comparison of the [PPy] data with the corresponding nanocomposite [PPyCNsF]^{NC} as isolated molecule indicated that (Wang et al. 2020; Al-Hossainy et al. 2020):

Table 4 Comparison data and calculated E_{HOMO}, E_{LUMO}, energy band gap (ΔE_g^{Opt}), chemical potential (μ), electronegativity (χ), global hardness (η), global softness (б) and global electrophilicity index (ω_1) for [PPy] and [PPyCNsF]^{NC} as isolated molecule

Compound	E_{HOMO}	E_{LUMO}	ΔE_g^{Opt}	χ	μ	η	S_1	ω_1	DN_{max}	σ	References
[PPy]	−5.047	−2.159	−2.888	3.603	−3.6	1.444	0.346	4.495	2.495	0.693	Present work
[PPyCNsF]^{NC}	−4.622	−3.014	−1.608	3.818	−3.82	0.804	0.622	9.065	4.749	1.244	Sanghvi et al. 2005
FSWCNT NP-SWNT-21	−5.00	−3.81	−1.19	4.405	−4.41	0.595	0.840	16.306	7.403	1.681	
NP-SWNT 49	−5.25	−3.67	−1.58	4.46	−4.46	0.790	0.633	12.589	5.646	1.266	Sedahmed et al. 2011
NP-SWNT 61	−5.63	−3.03	−2.60	4.33	−4.33	1.300	0.385	7.2111	3.331	0.769	
P(TBT)	−5.27	−3.42	−1.85	4.345	−4.35	0.925	0.541	10.205	4.697	1.081	Shuller-Nickles et al. 2014
P(TBT-Pt)	−5.31	−3.25	−2.06	4.28	−4.28	1.030	0.485	8.8924	4.155	0.971	

(a) The bond angles of the [PPy] as isolate molecule was decreased or enhanced due to the formation of six-membered chelate.
(b) The angles around the ion of metals correspond with the geometry of the octahedral.
(c) The bonds of the coordination sites become longer and weaker than that previously found in nanocomposite, e.g., C–OH, and/or C–O–C as a result of –O–[CNs]^{NPs} formation.
(d) There is a difference in C–O–C bond lengths of [PPy] and hybrid nanocomposite [PPyCNsF]^{NC} as isolated molecule attribute to the coordination gets place via O atoms of the (–C–O–C) ester group in [PPy].
(e) The data of [PPy] and hybrid nanocomposite [PPyCNsF]^{NC} as isolated molecules cleared that the lengths bonds –C–O–C– bonds are short than the lengths bonds –C–OH bonds (Badry et al. 2020; Eid and Al-Hossainy 2020).

The frontier molecular orbits were called HOMO (π-donor) and LUMO (π-acceptor) (FMOs). The energy transmitting correlation in the fragment is explained by the FMO vitality sources, E_{HOMO} and E_{LUMO}, in addition to the energy difference, ΔE_g^{Opt}, demonstrated in Fig. 8 (Ibrahim 2020; Thabet et al. 2020) and Table 4. The chemical reactivity descriptors similar to global softness (б), global electrophilicity index (ω_1) electronegativity (χ), global hardness (η), and chemical potential (μ) for the [PPy] and [PPyCNsF]^{NC} as isolated molecules were calculated. The obtained E_{HOMO} and E_{LUMO} were negative demonstrating the steadiness of these composites. The [PPy] and [PPyCNsF]^{NC} as isolated molecules revealed energy gap

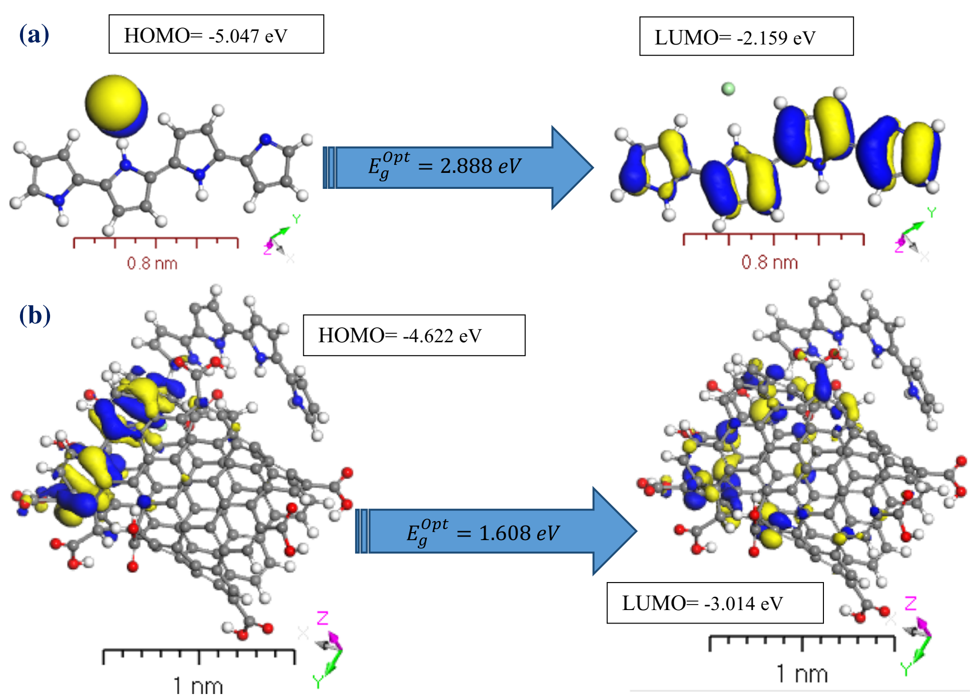

Fig. 8 The DFT computation used DMOl^3 Material studio software programs for **a** HOMO and LUMO calculations of the [PPY] and **b** HOMO and LUMO calculations of the [PPyCNs]^{NC}

value, ΔE_g^{Opt}, 2.888 and 1.616 eV, correspondingly, which showed their great energy enthusiasm and consequently high stability. The molecule's narrower energy difference makes it more polarizing and softer, as soft molecules are more reactive than hard molecules due to their ability to send an acceptor electron quickly. The electrophilicity index (ω_1) is used as the most fascinating quantum chemistry descriptor, because it indicates the toxicity of various contaminants and the biological function of drugs. It measures energy stability as the device receives additional electronic charges (El-Moussawi et al 2019, 2020; Wan et al. 2019; Ennehary et al. 2020; Al-Hossainy and Zoromba 2018).

Optical Properties of the thin film

The functional aspects of nonlinear optics (NLOs) are dominated by the interaction of electromagnetic radiation with matter; its interactions polarize the distribution of charge at the molecular level and change the field propagation. The linear approach is represented through polarization and nonlinear response through hyperpolarization. The optical properties study nonlinear optical property measurements on bulk systems, such as [PPy] and its hybrid nanocomposite $[PPyCNs]^{NC}$, with significant performance in the quantum chemistry and in such a way that the data can be included in the calibration of experiments. Figure 9a–d show the optical parameters

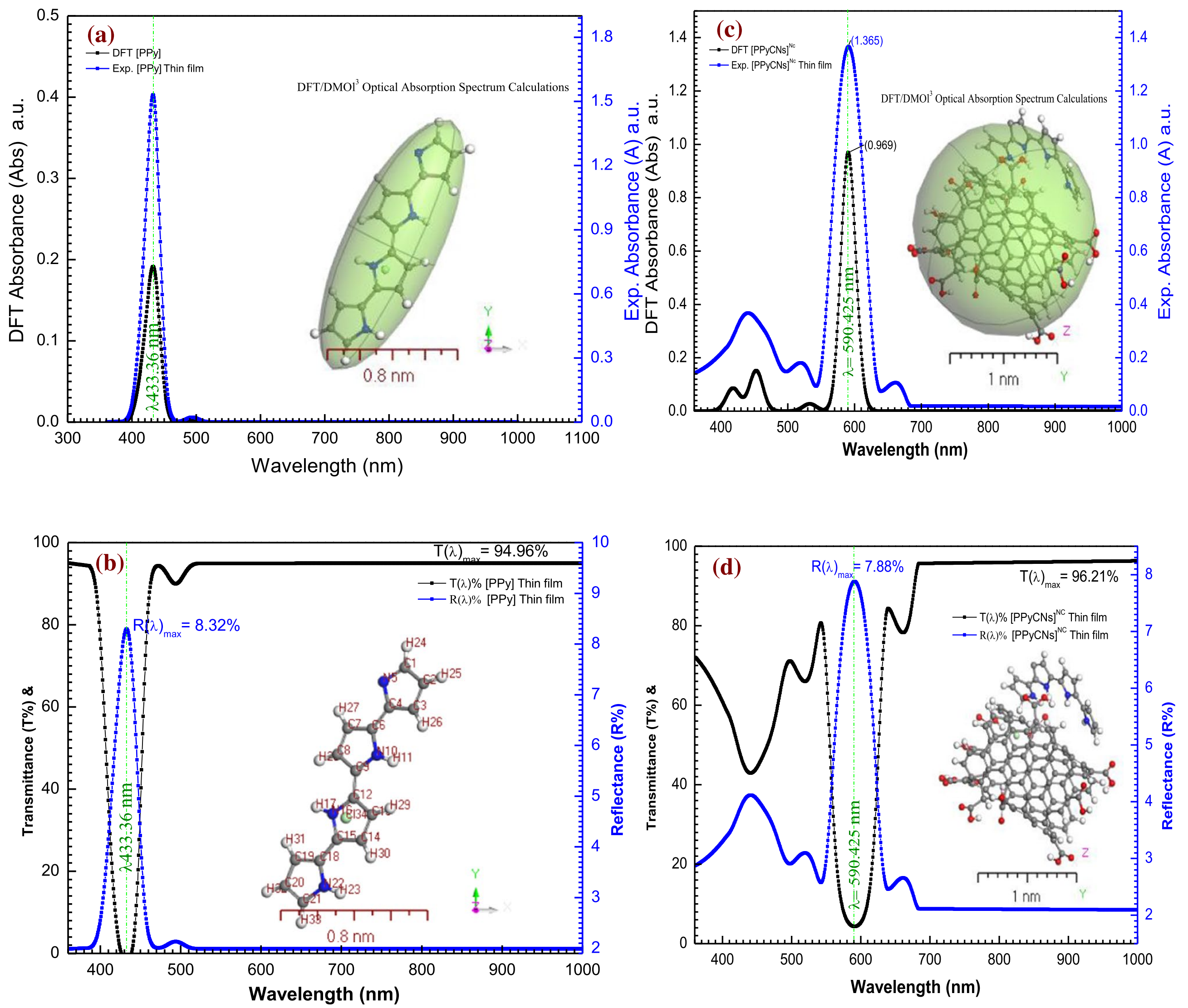

Fig. 9 **a** Absorbance (Abs) UV–Vis spectra for the simulated [PPy] and Experimental $[PPy]^{TF}$; **b** Transmittance T(λ)% and reflectance R(λ)% spectra for the Experimental $[PPy]^{TF}$; **c** Absorbance (Abs) UV–Vis spectra for the simulated [PPyCNs] and Experimental $[PPyCNs]^{NC}$. **d** Transmittance T(λ)% and reflectance R(λ)% spectra for the Experimental $[PPyCNs]^{NC}$

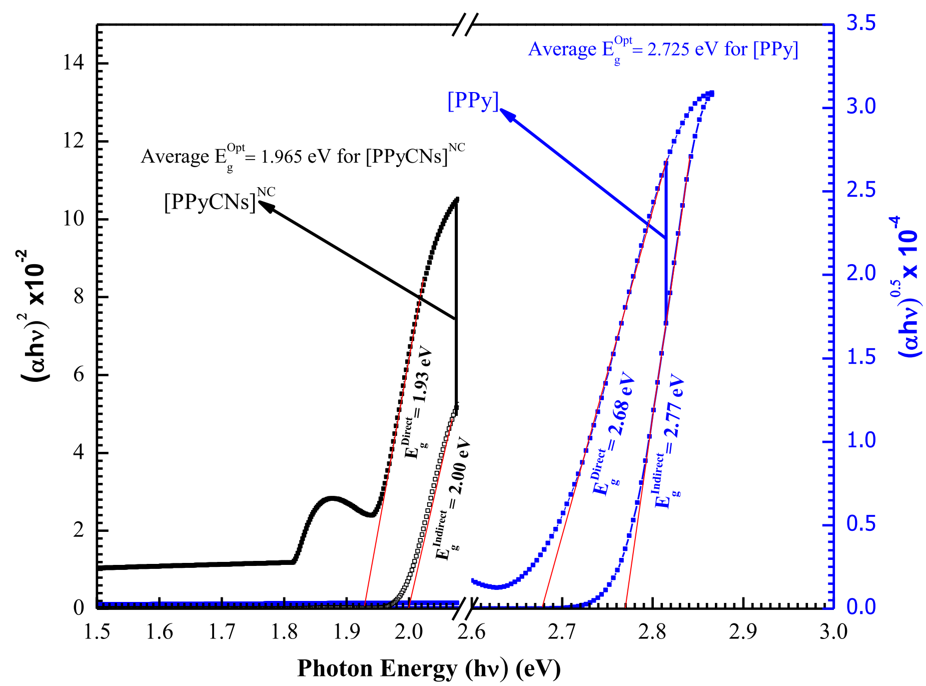

Fig. 10 Plot $(\alpha h\nu)^m$ vs photon energy (hν) eV for [PPy] and [PPyCNs]^{NC} as-deposited thin film

such as absorbance (Abs), transmittance (T(λ) %), and reflectance (T(λ) %) spectra of all simulated methods as an isolated molecule and experimental method as thin films. In Fig. 9a and c, the absorbance maximum value for [PPy] and [PPyCNsF]^{NC} thin films appear at λ_{max} = 433 nm and 590 nm. Thus, the two absorption bands for [PPy] and [PPyCNsF]^{NC} thin films are assigned to $\pi \rightarrow \pi^*$ shift, suggesting the occurrence of unsaturated C = O connections at 1109 cm^{-1} as stated in the FTIR. This again confirms the complexity and associations between the [CNs]^{NPs} and polymer chains. In Fig. 9b and d, the [PPy] polymer exhibits $T()_{max}$% at 94.98% and the nanocomposite films [PPyCNsF]^{NC} also show a reasonable $T()_{max}$% at 96.21% in most of the wavelength spectrum analyzed. The values of $T()_{max}$% confirm the creation of homogeneous composites that are ideal for optical applications of coating (Chen et al. 2017; Al-Hossainy 2016).

The electronic transition of the [PPy] and [PPyCNsF]^{NC} isolated molecules from HOMO to LUMO is related to this absorption band at 2.888 eV (λ = 429 nm) and 2.061 eV (λ = 601 nm), respectively (Navale et al. 2014; Al-Hossainy and Ibrahim 2015b). The absorption on the y-axis against wavelength on the x-axis for [PPy] and [PPyCNsF]^{NC} matrices by exploiting DMOl^3 in *DFT* scheming at 360 ≤ λ ≤ 1000 nm are shown in Fig. 9a and b. Two functions absorption bands were found for [PPy] and [PPyCNsF]^{NC} isolated molecules located at $_{max}$ = 433 nm and 590 nm due to π-π* shift as of optical properties. Conclude that, if a qualitative distinction is made, a strong consensus is detected for both simulated optical and experimental optical parameters between the computed DMOl^3.

To determine the E_g^{Opt} of the investigated materials in this work, Tauc's equation was used (Baishya 2018):

$$(\alpha hv)^2 = A\left(hv - E_g^{Opt}\right) \tag{3}$$

and

$$(\alpha hv)^{1/2} = A\left(hv - E_g^{Opt}\right) \tag{4}$$

for direct and indirect optical transformations, where A is a constant and hv is the approximated value of the incident photon energy

$$hv(eV) = 1242/\lambda(nm) \tag{5}$$

Figure 10a–b show the dependency of together $(\alpha hv)^2$ and $(\alpha hv)^{1/2}$ and on photon energy. Extending the linear parts of $(\alpha hv)^{1/2}$ and $(\alpha hv)^2$ curves to $\alpha = 0$ provide the indirect E_g^{Opt} and direct E_g^{Opt}, separately. The direct and indirect E_g^{Opt} of [PPy] thin-film are 2.68 and 2.77 eV, respectively, after loading [CNs]^{NPs} the direct and indirect E_g^{Opt} decreased to 1.93 and 2.00 eV, individually. The strong interactions between the [CNs]^{NPs} carboxylic group and [PPy] thin film are attributable to the discussed FTIR findings. Those thin films can therefore form load transfer complexes and cause defects in the [PPy] matrix. This complexation and enlarged disturbance, assisted by XRD findings, facilitates section movement of the chains and allows ion diffusion among the valence and lead bands of [PPy] (Ibrahim et al. 2020b; Gemeinera et al. 2015).

Conclusion

In situ oxidative polymerization is a suitable route for the preparation of doped polypyrrole/functionalized multi-walled carbon nanotubes composites $[PPyCNsF]^{NC}$. A surfactant such as sodium dodecyl sulfate can be used to control the morphology of the resulting nanocomposite. A thin film with controlled thickness can be prepared using the thermal evaporation technique. SEM photographs observed that the shape and size of the resulting polymer is depending on the type of used surfactant during the polymerization process and the presence of MWCNTs. The XRD obtained for the [PPy] and $[PPyCNsF]^{NC}$ thin films confirm that the material is nanocrystalline with the average crystallite size of 74.24 nm by using modified Scherer's equation. The increase in absorption bands from 433 to 590 nm in the UV/Vis region can be interpreted by π to π* transitions between bonding and anti-bonding molecular orbital for [PPy] and $[PPyCNsF]^{NC}$ thin films, respectively. The indirect optical transition for [PPy] and $[PPy\ NsF]^{NC}$ thin films is decreased from 2.77 to 2.00 eV for the fundamental energy bandgap, respectively. Optical thin-film characterizations demonstrated that optoelectronics and solar cell applications are excellent choices. The equal consensus between the theoretical and experimental findings of the present paper shows that a numerical approach is possible to forecast thin film features over a large range of conditions.

Acknowledgements This project was funded by the Deanship of Scientific Research (DSR) at King Abdulaziz University, Jeddah, under grant No. (G: 547-829-1441). The authors, therefore, acknowledge with thanks DSR for technical and financial support.

Declarations

Conflict of interest None of the authors of the manuscript has declared any conflict of interest.

References

Abdel-Aziz MH, Nirdosh I, Sedahmed GH (2013) Liquid–solid mass and heat transfer behavior of a concentric tube airlift reactor. Int J Heat Mass Transf 58:735–739. https://doi.org/10.1016/j.ijheatmasstransfer.2012.11.054

Abdel-Aziz MH, El-Ashtoukhy ESZ, Bassyouni M, Al-Hossainy AF, Fawzy EM, Abdel-Hamid SM, Zoromba MSh (2020a) DFT and experimental study on adsorption of dyes on activated carbon prepared from apple leaves. Carbon Letters. https://doi.org/10.1007/s42823-020-00187-1

Abdel-Aziz MH, Zoromba MSh, Bassyouni M, Zwawi M, Alshehri AA, Al-Hossainy AF (2020b) Synthesis and characterization of Co-Al mixed oxide nanoparticles via thermal decomposition route of layered double hydroxide. J Mol Struct 1206:127679. https://doi.org/10.1016/j.molstruc.2020.127679

Abd-Elmageed AAI, Ibrahim SM, Bourezgui A, Al-Hossainy AF (2020) Synthesis, DFT studies, fabrication, and optical characterization of the $[ZnCMC]^{TF}$ polymer (organic/inorganic) as an optoelectronic device. New J Chem 44:8621–8637. https://doi.org/10.1039/D0NJ01719A

Alcacer L (1987) Conducting Polymers, D *Reidel Publishing Company*, Dordrecht. Holland. https://doi.org/10.1007/978-94-009-3907-3

Al-Hossainy AF (2016) Synthesis, spectral, thermal, optical dispersion and dielectric properties of nanocrystalline dimer complex (PEPyr–diCd) thin films as novel organic semiconductor. Bull Mater Sci 39:209–222. https://doi.org/10.1007/s12034-015-1111-9

Al-Hossainy AF, Eid MR (2020) Structure, DFT calculations and heat transfer enhancement in $[ZnO/PG+ H_2O]^C$ hybrid nanofluid flow as a potential solar cell coolant application in a double-tube. J Mater Sci: Mater Electron 31:15243–15257. https://doi.org/10.1007/s10854-020-04089-w

Al-Hossainy AF, Ibrahim A (2015a) Synthesis, structural and optical properties of novel 3-(3, 5-dimethyl-1H-pyrazol-1-yl)-1-(diphenylphosphino)-2-((diphenylphosphino) methyl)-3-methylbutanone-1, 2-diphenylethane-1, 2-diamine tungsten dicarbonyl (PyrPMB-W) nanostructure thin film. Opt Mater 46:131–140. https://doi.org/10.1016/j.optmat.2015.04.011

Al-Hossainy AF, Ibrahim A (2015b) Structural, optical dispersion and dielectric properties of novel chromium nickel organic crystalline semiconductors. Mater Sci Semicond Process 38:13–23. https://doi.org/10.1016/j.mssp.2015.03.031

Al-Hossainy AF, Zoromba MSh (2018) New organic semiconductor thin film derived from p-toluidine monomer. J Mol Struct 1156:83–90. https://doi.org/10.1016/j.molstruc.2017.11.096

Al-Hossainy AF, Zoromba MSh, El-Gammal O, El-Dossoki FI (2019) Density functional theory for investigation of optical and spectroscopic properties of zinc-quinonoid complexes as semiconductor materials. Struct Chem 30:1365–1380. https://doi.org/10.1007/s11224-019-1289-3

Al-Hossainy AF, Abdelaal RM, El Sayed WN (2020) Novel synthesis, structure characterization, DFT and investigation of the optical properties of cyanine dye/zinc oxide $[4\text{-}CHMQI/ZnO]^C$ nanocomposite thin film. J Mol Struct 1224:128989. https://doi.org/10.1016/j.molstruc.2020.128989

Almutlaq N, Al-Hossainy AF (2020) Novel synthesis, structure characterization, DFT and investigation of the optical properties of diphenylphosphine compound/zinc oxide $[DPPB+ ZnO]^C$ nanocomposite thin film. Compos Interfaces. https://doi.org/10.1080/09276440.2020.1817682

Almutlaq N, Al-Hossainy A, Zoromba MSh (2021) Combined experimental and theoretical study, characterization, and nonlinear optical properties of doped-poly (p-nitroaniline-co-o-aminophenol) thin films. J Mol Struct 1227:129712. https://doi.org/10.1016/j.molstruc.2020.129712

Awad IM, Hassan FSM, Mohamed AE, Al-Hossainy AF (2004) Diphosphine compounds: part I. novel biologically active 1, 1′ bis-AND/OR 1, 2-cis-(diphenylphosphino-) ethene and their complexes [M (CO) n $\{Ph_2P\ (CH_n)_nPPh_2\}$] & [Cu $(Cl)_2\{Ph_2P\ (CH_n)$ $nPPh_2\}$],(M= W, Mo, Crn= 1, 2.... n). Phosphorus Sulfur Silicon 179:1251–1266. https://doi.org/10.1080/10426500490468074

Badr AM, El-Amin AM, Al-Hossainy AF (2006) Synthesis and optical properties for crystals of a novel organic semiconductor [Ni $(Cl)_2\{(Ph_2P)_2CHC\ (R_1R_2)\ NHNH_2\}$]. The Eur Phys J B-Condens Matter Complex Syst 53:439–448. https://doi.org/10.1140/epjb/e2006-00406-4

Badry R, Ibrahim A, Gamal F, Shehata D, Ezzat H, Elhaes H, Ibrahim M (2020) Electronic properties of polyvinyl alcohol/TiO_2/SiO_2 nanocomposites. Biointerface Res Appl Chem 10:6427–6435. https://doi.org/10.33263/BRIAC105.64276435

Baishya K, Ray JS, Dutta PJ, Das PP, Das SK (2018) Graphene-mediated band gap engineering of WO3 nanoparticle and a relook at Tauc equation for band gap evaluation. Appl Phys A 124:704. https://doi.org/10.1007/s00339-018-2097-0

Bersani M, Gupta K, Mishra AK, Lanza R, Taylor SR, Islam HU, Hollingsworth N, Hardacre C, De Leeuw NH, Darr JA (2016) Combined EXAFS, XRD, DRIFTS, and DFT study of nano copper-based catalysts for CO_2 hydrogenation. ACS Catal 6:5823–5833. https://doi.org/10.1021/acscatal.6b01529

Campbell TE, Hodgson AJ, Wallace GG (1999) Incorporation of erythrocytes into polypyrrole to form the basis of a biosensor to screen for rhesus (D) blood groups and rhesus (D) antibodies. Electroanalysis 11:215–222. https://doi.org/10.1002/(SICI)1521-4109(199904)11:4%3c215::AID-ELAN215%3e3.0.CO;2-%23

Chen Y, Li J, Tan L, Li Q (2017) Xia Zhang, Hui Xu, Electrodeposition of polypyrrole/functionalized-multiwalled carbon nanotubes composite and its application in supercapacitors. Electrochim Acta 258:43–50. https://doi.org/10.1016/j.electacta.2017.10.100

Cho JH, Yu JB, Kim JS, Sohn SO, Lee DD, Huh JS (2005) Sensing behaviors of polypyrrole sensor under humidity condition. Sens Actuators, B Chem 108:389–392. https://doi.org/10.1016/j.snb.2004.12.082

De S, Higgins TM, Lyons PE, Doherty EM, Nirmalraj PN, Blau WJ, Boland JJ, Coleman JN (2009) Silver nanowire networks as flexible, transparent, conducting films: extremely high DC to optical conductivity ratios. ACS Nano 3:1767–1774. https://doi.org/10.1021/nn900348c

Eid MR, Al-Hossainy AF (2020) Synthesis, DFT calculations, and heat transfer performance large-surface TiO2: ethylene glycol nanofluid and coolant applications. The Eur Phys J plus 135:596. https://doi.org/10.1140/epjp/s13360-020-00599-y

El-Ashtoukhy ESZ, Abdel-Aziz MH (2013) Removal of copper from aqueous solutions by cementation in a bubble column reactor fitted with horizontal screens. Int J Miner Process 121:65–69. https://doi.org/10.1016/j.minpro.2013.03.001

El-Moussawi Z, Nourdine A, Medlej H, Hamieh T, Chenevier P, Flandin L (2019) Fine tuning of optoelectronic properties of single-walled carbon nanotubes from conductors to semiconductors. Carbon 153:337–346. https://doi.org/10.1016/j.carbon.2019.07.023

El-Moussawi Z, Nourdine A, Flandin L (2020) A key progress in introducing single walled carbon nanotubes to photovoltaic devices. Appl Nanosci. https://doi.org/10.1007/s13204-020-01561-1

Endo M, Kim YA, Ezaka M, Osada K, Yanagisawa T, Hayashi T, Terrones M, Dresselhaus MS (2003) Selective and efficient impregnation of metal nanoparticles on cup-stacked-type carbon nanofibers. Nano Lett 3:723–726. https://doi.org/10.1021/nl034136h

Ennehary S, Toufik H, Bouzzine SM, Lamchouri F (2020) Effect of the alkyl chain length on the optoelectronic properties of organic dyes: theoretical approach. J Comput Electron 19:840–848. https://doi.org/10.1007/s10825-020-01486-6

Gangopadhyay R (2013) Peering into polypyrrole–SDS nanodispersions: rheological view. J Appl Polym Sci 128:1398–1408. https://doi.org/10.1002/app.38218

Gemeinera P, Kuliček J, Mikula M, Hatala M, Švorc Ľ, Hlavatá L, Mičušík M, Omastová M (2015) Polypyrrole-coated multi-walled carbon nanotubes for the simple preparation of counter electrodes in dye-sensitized solar cells. Synth Met 210:323–331. https://doi.org/10.1016/j.synthmet.2015.10.020

Gill PM, Johnson BG, Pople JA, Frisch MJ (1992) The performance of the Becke—Lee—Yang—Parr (B—LYP) density functional theory with various basis sets. Chem Phys Lett 197:499–505. https://doi.org/10.1016/0009-2614(92)85807-M

Grzelak A, Gawraczyński J, Jaroń T, Somayazulu M, Derzsi M, Struzhkin V, Grochala W (2017) Persistence of mixed and non-intermediate valence in the high-pressure structure of silver (I, III) Oxide, AgO: a combined raman, X-ray Diffraction (XRD), and density functional theory (DFT) study. Inorg Chem 56:5804–5812. https://doi.org/10.1021/acs.inorgchem.7b00405

Hashim A, Abduljalil H, Ahmed H (2020) Fabrication and characterization of (PVA-TiO_2) 1–x/SiCx nanocomposites for biomedical applications. Egypt J Chem 63:71–83. https://doi.org/10.21608/ejchem.2019.10712.1695

Heer W, Poncharal P, Berger C, Gezo J, Song Z, Bettini J, Ugarte D (2005) Liquid carbon, carbon-glass beads, and the crystallization of carbon nanotubes. Science 307:907–910. https://doi.org/10.1126/science.1107035

Ibrahim M (2020) Modeling the effect of Zinc Oxide on the electronic properties of polyvinyl alcohol. Egypt J Chem 63:3–5. https://doi.org/10.21608/ejchem.2020.27245.2564

Ibrahim SM, Al-Hossainy AF (2021) Synthesis, structural characterization, DFT, kinetics and mechanism of oxidation of bromothymol blue: application to textile industrial wastewater treatment. Chem Pap 75:297–309. https://doi.org/10.1007/s11696-020-01299-8

Ibrahim SM, Bourezgui A, Al-Hossainy AF (2020a) Novel synthesis, DFT and investigation of the optical and electrical properties of carboxymethyl cellulose/thiobarbituric acid/copper oxide [CMC+TBA/CuO]^C nanocomposite film. J Polym Res 27:1–18. https://doi.org/10.1007/s10965-020-02235-w

Ibrahim SM, Bourezgui A, Abd-Elmageed AAI, Kacem I, Al-Hossainy AF (2020b) Structural and optical characterization of novel [ZnKCMC]TF for optoelectronic device applications. J Mater Sci: Mater Electron 31:8690–8704. https://doi.org/10.1007/s10854-020-03404-9

Iroh JO, Williams C (1999) Formation of thermally stable polypyrrole-naphthalene/benzene sulfonate-carbon fiber composites by an electrochemical process. Synth Met 99:1–8. https://doi.org/10.1016/S0379-6779(98)00160-X

Jiang L, Jun HK, Hoh YS, Lim JO, Lee DD, Huh JS (2005) Sensing characteristics of polypyrrole–poly (vinyl alcohol) methanol sensors prepared by in situ vapor state polymerization. Sens Actuators, B Chem 105:132–137. https://doi.org/10.1016/j.snb.2003.12.077

Kampf AR, Hughes JM, Nash BP, Wright SE, Rossman GR, Marty J (2014) Ophirite, Ca2Mg4 [Zn2Mn23+ (H2O) 2 (Fe3+ W9O34) 2]· 46H2O, a new mineral with a heteropolytungstate tri-lacunary Keggin anion. Am Miner 99:1045–1051. https://doi.org/10.2138/am.2014.4699

Kemp NT, Fianagan GU, Kaiser AB, Trodahl HJ, Chapman B, Partridge AC, Buckley RG (1999) Temperature-dependent conductivity of conducting polymers exposed to gases. Synth Met 101:434–435. https://doi.org/10.1016/S0379-6779(98)01118-7

Kincal D, Kumar A, Child AD, Reynolds JR (1998) Conductivity switching in polypyrrole-coated textile fabrics as gas sensors. Synth Met 92:53–56. https://doi.org/10.1016/S0379-6779(98)80022-2

Krishnaswamy S, Ragupathi V, Raman S, Panigrahi P, Nagarajan GS (2019) Optical properties of P-type polypyrrole thin film synthesized by pulse laser deposition technique: hole transport layer in electroluminescence devices. Optik 194:163034. https://doi.org/10.1016/j.ijleo.2019.163034

Liang L, Chen G, Guo CY (2017) Polypyrrole nanostructures and their thermoelectric performance. Mater Chem Front 1:380–386. https://doi.org/10.1039/C6QM00061D

Lim SP, Shahid MM, Rameshkumar P, Huang NM, Che L (2020) Amperometric detection of hydrogen peroxide and its density functional theory for adsorption on Ag/TiO_2 nanohybrid. J Mater Sci: Mater Electron 31:6017–6026. https://doi.org/10.1007/s10854-020-03153-9

Lin TT, Liu XY, He C (2010) A DFT study on poly (lactic acid) polymorphs. Polymer 51:2779–2785. https://doi.org/10.1016/j.polymer.2010.03.062

Liu X, Ly J, Han S, Zhang DH, Requicha A, Thompson ME, Zhou C (2005) Synthesis and electronic properties of individual single walled carbon nanotube/polypyrrole composite nanocables. Adv Mater 17:2727–2732. https://doi.org/10.1002/adma.200501211

Ma Y, Cheung W, Wei D, Bogozi A, Chiu PL, Wang L, Pontoriero F, Mendelsohn R, He H (2008) Improved conductivity of carbon nanotube networks by in situ polymerization of a thin skin of conducting polymer. ACS Nano 2:1197–1204. https://doi.org/10.1021/nn800201n

Mahmoud SA, Al-Dumiri AA, Al-Hossainy AF (2020) Combined experimental and DFT-TDDFT computational studies of doped [PoDA+ PpT/ZrO2] C nanofiber composites and its applications. Vacuum 182:109777. https://doi.org/10.1016/j.vacuum.2020.109777

Mohlala LM, Jen TC, Olubambi PA (2020) Thermal stability and reactivity of titanium halide precursors for the atomic layer deposition of TiO_2 on a Pt (111) surface. Procedia CIRP 93:9–13. https://doi.org/10.1016/j.procir.2020.05.156

Munish P, Badlani R (2019) Ac conductivity and dielectric studies of polypyrrole-papain composite. Int J Res 7:332–338. https://doi.org/10.29121/granthaalayah.v7.i8.2019.681

Navale ST, Mane AT, Ghanwat AA, Mulik AR, Patil VB (2014) Camphor sulfonic acid (CSA) doped polypyrrole (PPy) films: measurement of microstructural and optoelectronic properties. Measurement 50:363–369. https://doi.org/10.1016/j.measurement.2014.01.012

Rajeh A, Morsi M, Elashmawi I (2019) Enhancement of spectroscopic, thermal, electrical and morphological properties of polyethylene oxide/carboxymethyl cellulose blends: combined FT-IR/DFT. Vacuum 159:430–440. https://doi.org/10.1016/j.vacuum.2018.10.066

Reddy CV, Reddy IN, Reddy KR, Jaesool S, Yoo K (2019) Template-free synthesis of tetragonal Co-doped ZrO_2 nanoparticles for applications in electrochemical energy storage and water treatment. Electrochim Acta 317:416–426. https://doi.org/10.1016/j.electacta.2019.06.010

Sanghvi AB, Miller KPH, Belcher AM, Schmidt CE (2005) Biomaterials functionalization using a novel peptide that selectively binds to a conducting polymer. Nat Mater 4:496–502. https://doi.org/10.1038/nmat1397

Sedahmed GH, El-Taweel YA, Konsowa AH, Abdel-Aziz MH (2011) Mass transfer intensification in an annular electrochemical reactor by an inert fixed bed under various hydrodynamic conditions. Chem Eng Process 50:1122–1127. https://doi.org/10.1016/j.cep.2011.10.002

Shuller-Nickles LC, Bender WM, Walker SM, Becker U (2014) Quantum-mechanical methods for quantifying incorporation of contaminants in proximal minerals. Minerals 4:690–715. https://doi.org/10.3390/min4030690

Siwal SS, Zhang Q, Devi N, Thakur VK (2020) Carbon-based polymer nanocomposite for high-performance energy storage applications. Polymers 12:505. https://doi.org/10.3390/polym12030505

Smela E (1999) Microfabrication of PPy microactuators and other conjugated polymer devices. J Micromech Microeng 9:1. https://doi.org/10.1088/0960-1317/9/1/001

Thabet HK, Al-Hossainy AF, Imran M (2020) Synthesis, characterization, and DFT modeling of novel organic compound thin films derived from 2-amino-4-(2-hydroxy-3-methoxyphenyl)-4H-thiazolo [3, 2-a][1, 3, 5] triazin-6 (7H)-one. Opt Mater 105:109915. https://doi.org/10.1016/j.optmat.2020.109915

Torraca PL, Bobinger M, Servadio M, Pavan P, Becherer M, Lugli P, Larcher L (2018) On the frequency response of nanostructured thermoacoustic loudspeakers. Nanomaterials 8:833. https://doi.org/10.3390/nano8100833

Veved A, Ejuh GW, Djongyang N (2020) Study of the optoelectronic and piezoelectric properties of ZrO2 doped PVDF from quantum chemistry calculations. Chin J Phys 63:213–219. https://doi.org/10.1016/j.cjph.2019.10.022

Vidal JC, García E, Castillo JR (1999) In situ preparation of a cholesterol biosensor: entrapment of cholesterol oxidase in an overoxidized polypyrrole film electrodeposited in a flow system: determination of total cholesterol in serum. Anal Chim Acta 385:213–222. https://doi.org/10.1016/S0003-2670(98)00838-1

Wan T, Yin X, Pan C, Liu D, Zhou X, Gao C, Wong W, Wang L (2019) Boosting the adhesivity of π-conjugated polymers by embedding platinum acetylides towards high-performance thermoelectric composites. Polymers 11:593. https://doi.org/10.3390/polym11040593

Wang J, Dai J, Yarlagadda T (2005) Carbon nanotube−conducting-polymer composite nanowires. Langmuir 21:9–12. https://doi.org/10.1021/la0475977

Wang B, Cui GY, Zhang BB, Li Z, Ma HX, Wang W, Zhang FY, Ma XX (2020) Novel axial substituted subphthalocyanine and its TiO_2 photocatalyst for degradation of organic water pollutant under visible light. Opt Mater 109:110202. https://doi.org/10.1016/j.optmat.2020.110202

Yadav AA, Kulkarni SB, Lokhande CD (2018) Synthesis and characterization of polypyrrole thin film by MW-CBD method for NH 3 gas sensor. Polym Bull 75:4547–4553. https://doi.org/10.1007/s00289-018-2282-5

Zhang B, Xu Y, Zheng Y, Dai L, Zhang M, Yang J, Chen Y, Chen X, Zhou J (2011) A facile synthesis of polypyrrole/carbon nanotube composites with ultrathin, uniform and thickness-tunable polypyrrole shells. Nanoscale Res Lett 6:1–9. https://doi.org/10.1186/1556-276X-6-431

Zoromba MSh, Bassyouni M, Abdel-Aziz MH, Al-Hossainy AF, Salah N, Al-Ghamdi AA, Eid MR (2019) Structure and photoluminescence characteristics of mixed nickel–chromium oxides nanostructures. Appl Phys A 125:642. https://doi.org/10.1007/s00339-019-2933-x